IMPORTANCE OF STRUCTURAL DAMPING IN THE DYNAMIC ANALYSIS OF COMPLIANT DEPLOYABLE STRUCTURES

Florence Dewalque
Department of Aerospace and Mechanical Engineering (LTAS), University of Liège, Belgium, f.dewalque@ulg.ac.be

Pierre Rochus, Centre Spatial de Liège, University of Liège, Belgium, prochus@ulg.ac.be
Olivier Brüls, LTAS, University of Liège, Belgium, o.bruls@ulg.ac.be

Abstract

Compliant mechanisms such as tape springs are often used on satellites to deploy appendices, e.g. solar panels, antennas, telescopes and solar sails. Their main advantage comes from the fact that their motion results from the elastic deformation of structural components and the absence of actuators or external energy sources. The mechanical behaviour of a tape spring is intrinsically complex and nonlinear involving buckling, hysteresis and self-locking phenomena. In the majority of the previous works, dynamic simulations were performed without any physical representation of the structural damping. These simulations could be successfully achieved because of the presence of numerical damping in the transient solver. However, in this case, the dynamic response turns out to be quite sensitive to the amount of numerical dissipation, so that the predictive capabilities of the model are questionable. In this work based on numerical case studies, we show that the dynamic simulation of a tape spring can be made less sensitive to numerical parameters when the structural dissipation is taken into account.

I INTRODUCTION

With the extensive development of small satellites and cubesats dedicated to low-cost missions, the mass reduction of the components is paramount. However, the power reduction due to the miniaturisation of electronic equipment does not follow the same downward slope. Thus, covering only the external surface of the satellite with solar cells might not provide enough power and be too restrictive, hence the necessity for a reliable but cheap and simple means to deploy large solar panels. This, however, brings another major problem that must be solved: the packaging of large structures into the confined space inside the fairing of launch vehicles. In order to address these challenges, deployable structures have been developed and a brief listing of the most common structures can be found in [1]. This paper will focus on those belonging to the compliant mechanisms category and in particular on tape springs.

A tape spring is a thin strip curved along its width commonly known as a Carpenter tape and used in the everyday life as tape measures. Nowadays, it finds applications in the space domain for the deployment of appendices such as solar panels, antennas, telescopes and solar sails. Since they belong to the category of compliant mechanisms, they rely only on elastic energy that is stored during the folding and then naturally released when deployed. Indeed, a possible equilibrium state when the tape spring is free of constraints is the straight configuration, which is sought as a deployed configuration for many space applications. This characteristic also brings forward the fact that no source of external energy is required for the deployment and hence the passive and self-actuated behaviours of these devices.

Their motion results from the deformation of structural components only and not from the sliding between contact surfaces as in usual hinges or prismatic joints. It implies that tape springs do not require any lubricant to ensure a motion without jamming, which is advantageous in order to avoid outgassing and contamination in space. The structural simplicity of tape springs is also beneficial, since, without taking into account the supports, a tape spring consists of a single component and thus does not require any assembly procedure. The robustness is then greatly improved compared to more common mechanisms and it limits the possibilities of failure during deployment.

Regarding the mechanical behaviour of tape springs, it is complex and highly nonlinear, but stays in the elastic regime for the most commonly used materials such as BeCu. Regarding other materials, a limit that the ratio between the transverse radius and the thickness must satisfy can be found in [2] to avoid any plastic deformation during folding.

The complexity is further increased due to the existence of nonlinear phenomena such as buckling which induces the formation of a fold in the deformed configuration and the non-superposition of the loading and unloading paths leading to hysteresis and self-locking.

The mathematical background describing the theoret-

ical relationship between the rotation angle and the resulting bending moment was first developed by authors such as Wüst [3], Rimrott [4] and Mansfield [5]. More recently, new analytical models were combined to numerical studies and experiments for validation. In [6], the static bending moment-angle relationship was numerically computed for a large variety of tape springs. In a next work [7], the dynamic deployment was investigated and it allowed representing a folded tape spring as two rigid bodies of variable length connected to each other with a mobile hinge. Between this 2D discrete model and finite element simulations with shells, an intermediate model was developed in [8] based on 1D planar rods with a flexible cross-section. Quasi-static analyses of the folded configuration submitted to end loads were also performed in [9] and correctly predicted thanks to a variational technique. Finally, more complex and compact three dimensional foldings can be obtained and were studied, first analytically in [10], then experimentally in [11, 12].

Tape springs can also be combined to form tape spring hinges [13]. A generic one called MAEVA was developed by the CNES and 01dB-Metravib [14] and was successfully used to deploy solar panels, antennas and masts on the six MYRIADE micro-satellites [15]. Experimental analyses were performed, along with finite element simulations. Recently, a more precise study of the dynamic behaviour and the self-locking phenomenon was carried out in [16].

In the majority of the previous works, finite element dynamic simulations of tape springs were performed without any physical representation of the structural damping, with the notable exceptions of [17, 18]. In the former, the viscoelastic material properties of a reinforced polymer are integrated in the finite element model under the form of a Prony series. The goal was to determine the impact of the temperature, the folding rate, the creep recovery and the relaxation during stowage on the behaviour of the tape spring. On the other hand, [18] does not directly concern tape springs, but analyses foldable flattenable tubes which are also characterised by buckling and hysteresis phenomena. The structural damping is in this case based on the Rayleigh model with the particularity that the damping factor is variable according to the state of the structure. Otherwise, the simulations could be successfully achieved because of the presence of numerical damping in the transient solvers. However, as it will be proven further in this paper, the dynamic response turns out to be quite sensitive to the amount of numerical dissipation. The predictive capabilities of the models are then questionable. Furthermore, in the analytical model developed in [7], it was shown that viscous damping terms needed to be introduced in order to match the numerical results to the experiments. The aim of this work is then to determine if adding structural damping can make the simulator less sensitive and if numerical damping is always required. The choice is made to represent the structural dissipation by Kelvin-Voigt models in order to keep the simulations as simple as possible.

The layout of this paper is as follows. In Section II, the geometric characteristics of a tape spring are described. Then in Section III, the general features of the finite element models and the resolution strategy are explained. In Section IV, the theory ruling the bending behaviour of tape springs is recalled. In Section V, the effect of numerical and structural dampings in the generalized-α method is analysed on a one-degree-of-freedom model and compared to the analytical solution. In Section VI, the impact of the numerical damping on the bending behaviour of a tape spring is studied in the case of a dynamic deployment. In Section VII, structural damping is added in the same model. Finally, the conclusions of this work are drawn in Section VIII.

II GEOMETRIC CHARACTERISTICS

The geometry of a tape spring is defined by the means of five parameters: its length L, its thickness t, its subtended angle α, its transverse radius of curvature R and its longitudinal radius of curvature R_L. All these elements are represented in Figure 1.

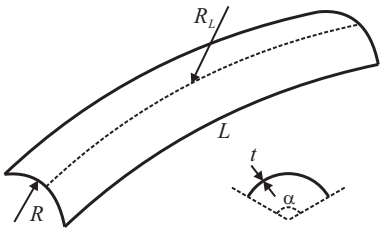

Figure 1: Geometric characteristics of a tape spring with the length L, the thickness t, the subtended angle α, the transverse radius of curvature R and the longitudinal radius of curvature R_L.

For the most common applications and the structures studied in this paper, the tape springs are straight without any longitudinal curvature. In other cases, they would be referred to as curved tape springs [19].

Regarding the ratio between the length and the width,

a lower limit of five will be respected in order to reduce the local end effects due to the boundary conditions [5].

III FINITE ELEMENT MODELS

All the finite element models in this paper are developed in the commercial software SAMCEF [20]. Since the thickness of a tape spring can be several orders of magnitude smaller than its other dimensions, the finite elements are linear shells based on the Mindlin-Reissner theory available in the software. Parabolic shells were also tested, but they did not have a significant impact on the results and the computational cost was unnecessarily increased.

Regarding the size of the mesh, a campaign of tests led to the choice of elements of 3 *mm* as the default size, for which all the key parameters describing a tape spring's behaviour have converged. However, in some particular cases, another size might be used and will be clearly specified.

Furthermore, nodes are added at the centroids of the cross-sections located at the extremities of the tape spring to which they are rigidly connected along the whole width. Their purpose is to give an easy means to control the angle of bending, to apply the boundary conditions and to determine the resulting bending moment.

The problems will be solved in two consecutive steps. First, starting from the equilibrium state corresponding to the straight configuration, the tape spring is folded to the required bending angle by performing a very slow dynamic analysis. Although static analyses taking the form of continuation methods can be exploited in this first part, the algorithm is quite sensitive to the parameters and severely increases the computation cost. As a consequence, they are not used in this work. A comparison between the static and dynamic results can be found in [16], which shows that the two approaches give very close results. Then, once the deformed configuration is stabilised, the structure is released and simulated with a standard dynamic analysis. In both situations, the following time step algorithms can be exploited: Newmark [21] of first-order accuracy, HHT [22] and generalized-α [23] both of second-order accuracy. However, only the former and the latter will be used in this work since it was observed that the HHT and generalized-α methods give similar results for the bending of tape springs [16]. Regarding the time step, an adaptive method is exploited in order to accurately capture the nonlinear phenomena and reduce the computation costs when the deformed configuration does not significantly evolve.

IV BENDING BEHAVIOUR OF A TAPE SPRING

IV.I Theoretical behaviour

The bending behaviour of a tape spring is direction dependent. The senses of bending were first defined by Wüst [3] and are represented in Figure 2 where the sign conventions for the bending moment M and the bending angle θ are also visible.

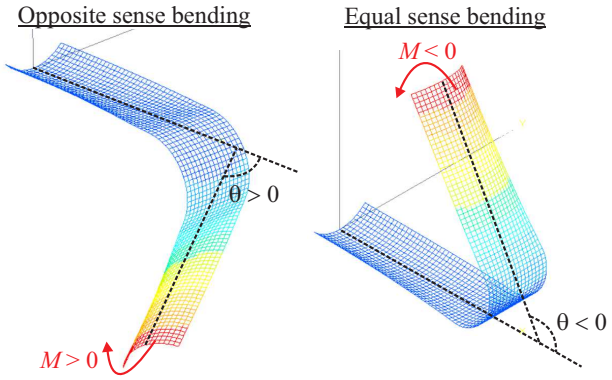

Figure 2: Senses of bending and sign conventions with M the bending moment and θ the bending angle.

The opposite sense bending is characterised by longitudinal and transverse curvatures in opposite sense. It induces tensile stresses along the edges and only bending efforts appear during the deformation.

On the contrary, for the equal sense bending, the longitudinal and transverse curvatures are in the same sense and it induces compressive stresses along the edges. However, the deformed configuration is characterised by flexural-torsional modes, thus bringing forward the complex behaviour resulting from this sense of bending.

The evolution of the deformed configuration of a tape spring when submitted to opposite or equal sense bending and for the folding or the deployment of the structure can be explained with the help of the schematic diagram in Figure 3 inspired from [6], which gives the corresponding bending moment when the tape spring is controlled in rotation through the bending angle.

Starting from the origin O and in the opposite sense, the bending moment first varies linearly with the bending angle for small rotations. The associated deformed configuration corresponds to a tape spring bended into a smooth curve. Then, for larger rotations, the increasing M forces the cross section to flatten, especially in the middle, un-

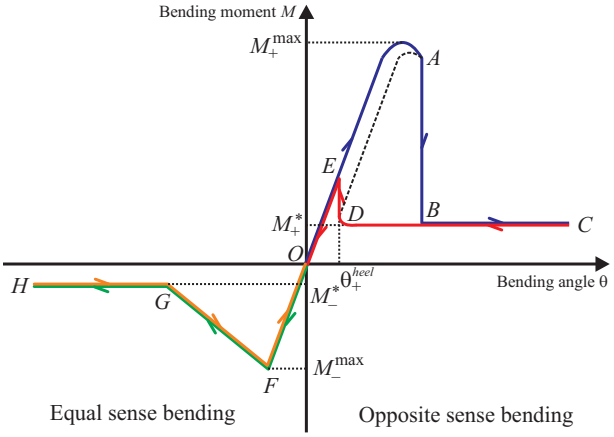

Figure 3: Bending moment-angle diagram. Blue (*OABC*): loading in opposite sense; red (*CDEO*): unloading in opposite sense; green (*OFGH*): loading in equal sense; orange (*HGFO*): unloading in equal sense; dashed line (*AD*): unstable path.

til it reaches a maximum: the peak moment M_+^{max}. Right after this critical value, the structure is submitted to buckling and a fold forms in the middle. It can be theoretically proven that the radius of curvature of the fold is equal to the initial transverse curvature of the tape spring [3, 24]. However, finite element studies showed that a difference exists between the two values, but it is marginal [2]. The buckling is then accompanied by an important decrease in the bending moment represented on the diagram by the vertical line *AB*. In the particular case where the unstable equilibrium can be captured, the path defined by the curve *AD* is followed. If the rotation between the extremities is further increased (*BC*), the bending moment remains approximately constant to M_+^* called the steady-state moment.

In the reverse direction which represents the deployment of the tape spring, the same path as for the folding is first followed (*CB*). At point *B*, the bending moment does not go back to point *A*, but stays constant until it reaches point *D* called the heel. There, the curve jumps to point *E* where one can notice that the associated bending moment is smaller than the peak moment M_+^{max}. For the last part (*EO*), the linear behaviour is recovered.

The difference between the paths for the folding and the deployment is responsible for the hysteresis phenomenon, which itself, through the dissipation of energy, will lead to the self-locking of the tape spring.

For the equal sense bending and small rotations, M also varies linearly with θ as in the opposite sense. Furthermore, the slope of *OF* is equal to the slope of *OE*. However, in this case, the linear behaviour ends up much sooner. Buckling happens at point *F* for another critical value such that $|M_-^{max}| < |M_+^{max}|$. Regarding the deformed configuration, the buckling appears when asymmetric torsional folds created at the extremities combine themselves at the middle of the tape spring to form a symmetric one as the one described in opposite sense. Then, for the rest of the folding (*GH*), the bending moment remains constant (M_-^*).

Finally, in equal sense bending, it is commonly assumed that the deployment path is superimposed on the folding path.

IV.II Finite element analysis

In order to show that the commercial software SAMCEF is able to capture the key parameters of a tape spring's behaviour, the structure with the geometric and material characteristics specified in Table 1 is analysed.

L	t	α	R
200 *mm*	0.1 *mm*	90°	20 *mm*
E	ν	ρ	
131000 *MPa*	0.3	8100 kg/m^3	

Table 1: Geometric and material characteristics of the tape spring analysed in SAMCEF and [6].

To perform the simulation, one of the nodes located at the centroids is clamped, while on the other one, the bending angle is controlled and the displacements in the transverse direction are locked in order to guide the deformation without restraining the torsion. The mesh size is fixed to 1 *mm*. Regarding the time integration scheme, as discussed in Section III, the Newmark method [21] is chosen with a variable time step selection procedure. This strategy allows us to have a small time step during the nonlinear phenomena such as buckling and a larger one when the deformed configuration slightly evolves. A numerical damping defined by the spectral radius at infinite frequencies is introduced and is equal to zero in order to annihilate the oscillations after buckling in a minimum number of time steps. The results are given in Figure 4 where the artificial vertical peaks occurring during the buckling phenomena are due to the transient behaviour of the solution.

For the loading in the opposite sense (blue ∘-curve), all the characteristic features are well represented by the model: the linear behaviour for small rotations, the peak moment M_+^{max} followed by the buckling of the structure and a steady-state moment M_+^*. During the unloading (red

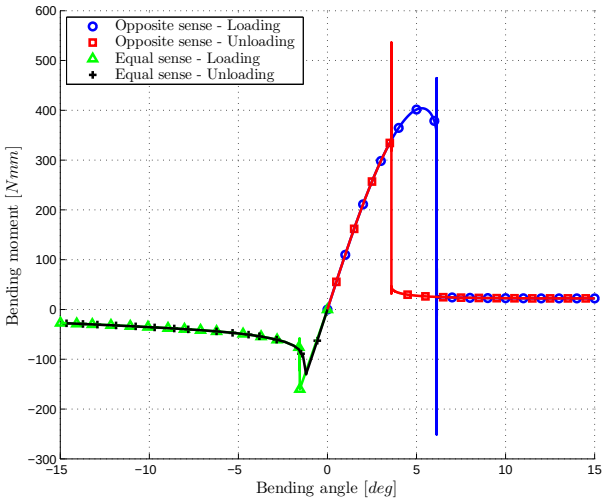

Figure 4: Bending moment-angle behaviour from SAMCEF with the characteristics of Table 1.

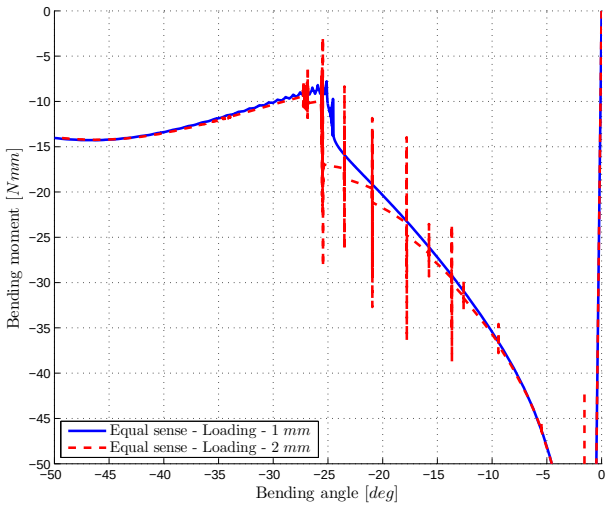

Figure 5: Vertical zoom on the loading part in equal sense bending form the mesh sizes 1 *mm* and 2 *mm*.

□-curve), the bending moment jumps back on the loading curve for a smaller bending angle than the one at which buckling occurred. Thus the hysteresis phenomenon is well captured.

Regarding the loading (green △-curve) and unloading (black +-curve) paths in the equal sense, they are almost identical and are characterised by a peak moment $M_{-}^{\max}$ and a steady-state moment M_{-}^{*} for larger rotations. Furthermore, the slope in the linear zone is equivalent to the one created in opposite sense bending. As it was mentioned before, the equal sense bending leads to a more complex behaviour due to flexural-torsional modes. It results in a series of disruptive oscillations in the $M(\theta)$ curve whose amplitude increases with the mesh size (Figure 5). However, the mean behaviour of the curve associated to a mesh size of 2 *mm* still matches the reference curve obtained with a mesh size of 1 *mm*. Notice that the peak moment $M_{-}^{\max}$ is truncated on the plot in order to focus on these oscillations.

Regarding the quantitative accuracy of the software, the results displayed in Figure 4 fairly reproduce those numerically obtained by Seffen in [6]. Compared to experimental investigations in [11] on two dimensional folds with the characteristics of Table 2, the average peak moment and steady-state moment in opposite sense bending are obtained with a difference of 5.34 % and 1.91 % respectively. However, for smaller lengths, the correlation for the peak moment is far less effective due to end effects. Indeed, Seffen [7] showed by comparing analytical, experimental and numerical results for a same tape spring that the peak moment can strongly differ for short tape springs, while the steady-state moment is not affected.

L	t	α	R
433 *mm*	0.11459 *mm*	1.719 *rad*	15.37 *mm*

E	ν	ρ
195300 *MPa*	0.3	8100 kg/m^3

Table 2: Geometric and material characteristics of the tape spring experimentally analysed in [11].

V DISSIPATION IN THE GENERALIZED-α METHOD

In order to have a better understanding of the influence of structural and numerical dampings in the most common time integration schemes (Newmark, HHT, generalized-α), a simple example will be studied: the mass-spring-damper system (Figure 6). All these methods are characterised by a controllable numerical damping, the first goal of which is to take part in the dissipation of high frequencies. Indeed, when a structure is discretized by the means of a finite element model, the high frequency modes are poorly represented and must be filtered in order to improve the quality of the system's response, while the low frequency modes must remain unaffected by the damping. Furthermore, the introduction of numerical damping in these methods ensures a better convergence of the algorithm, especially in the case of nonlinear systems.

It can be easily shown that the Newmark and HHT

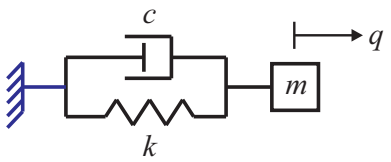

Figure 6: Mass m – spring k – damper c system.

methods are particular cases of the generalized-α method. This latter will then be used in the next developments and the specific values of the parameters to recover the other methods will be recalled.

The generalized-α method relies on the following update formulae [23]:

$$\mathbf{M}(\mathbf{q}_{n+1})\ddot{\mathbf{q}}_{n+1} + \mathbf{g}(\mathbf{q}_{n+1}, \dot{\mathbf{q}}_{n+1}, t_{n+1}) = 0 \quad (1)$$

$$\mathbf{q}_{n+1} = \mathbf{q}_n + h\dot{\mathbf{q}}_n + h^2(0.5-\beta)\mathbf{a}_n + h^2\beta\mathbf{a}_{n+1} \quad (2)$$

$$h\dot{\mathbf{q}}_{n+1} = h\dot{\mathbf{q}}_n + h^2(1-\gamma)\mathbf{a}_n + h^2\gamma\mathbf{a}_{n+1} \quad (3)$$

$$(1-\alpha_m)h^2\mathbf{a}_{n+1} + \alpha_m h^2\mathbf{a}_n = (1-\alpha_f)h^2\ddot{\mathbf{q}}_{n+1} + \alpha_f h^2\ddot{\mathbf{q}}_n \quad (4)$$

where the first equation is a general equation of motion, $\mathbf{q}$ is the vector of degrees of freedom, $\mathbf{M}$ is the mass matrix, $\mathbf{g}$ is the vector of external forces, t is the time, h is the time step, $\mathbf{a}$ is an acceleration-like variable which approximates the physical acceleration $\ddot{\mathbf{q}}$ at an intermediate time as $\mathbf{a}_n \simeq \ddot{\mathbf{q}}(t_n + h(\alpha_m - \alpha_f))$ and $\beta, \gamma, \alpha_m, \alpha_f$ are numerical parameters. The Newmark method is recovered when $\alpha_f = \alpha_m = 0$, while the HHT method requires to have $\alpha_m = 0$, $\alpha_f \in [0, 1/3]$, $\gamma = 0.5 + \alpha_f$ and $\beta = 0.25(\gamma + 0.5)^2$.

For the generalized-α method, the numerical damping is controlled through the spectral radius at infinite frequencies ρ_∞ which belongs to the interval $[0,1]$ according to:

$$\alpha_m = \frac{2\rho_\infty - 1}{\rho_\infty + 1} \quad \text{and} \quad \alpha_f = \frac{\rho_\infty}{\rho_\infty + 1} \quad (5)$$

When $\rho_\infty = 0$, the dissipation leads to a complete annihilation of the high frequency content and, on the opposite, when $\rho_\infty = 1$ there is no dissipation.

In order to assess the level of dissipation, the spectral radius is used. It is defined as:

$$\rho = \max(|\lambda_1|, |\lambda_2|, |\lambda_3|) \quad (6)$$

where the $\lambda_i (i = 1,2,3)$ are the eigenvalues of the amplification matrix of the system. If the value of the spectral radius is low on a specific range of frequencies, then the system is submitted to dissipation on this range.

The equation of motion of the mass-spring-damper system without any applied force is given by:

$$m\ddot{q} + c\dot{q} + kq = 0 \quad (7)$$

with q the degree of freedom, m the mass, k the spring's stiffness and c the damper's damping (Figure 6). It can be reformulated by making use of the natural pulsation $\omega^2 = \frac{k}{m}$ and the structural damping $\varepsilon = \frac{c}{2\omega m}$ as:

$$\ddot{q}_{n+1} + 2\varepsilon\omega\dot{q}_{n+1} + \omega^2 q_{n+1} = 0 \quad (8)$$

The system of equations Eqs. (2)–(4), together with the equation of motion Eq. (8), can be transformed into the following matrix form:

$$\mathbf{E}\mathbf{x}_{n+1} = \mathbf{B}\mathbf{x}_n \quad (9)$$

with $\mathbf{x}_i = \begin{pmatrix} q_i & h\dot{q}_i & h^2 a_i \end{pmatrix}^T$ and the matrices:

$$\mathbf{E} = \begin{pmatrix} 1 & 0 & -\beta \\ 0 & 1 & -\gamma \\ (1-\alpha_f)\omega^2 h^2 & (1-\alpha_f)2\varepsilon\omega h & 1-\alpha_m \end{pmatrix} \quad (10)$$

$$\mathbf{B} = \begin{pmatrix} 1 & 1 & 0.5-\beta \\ 0 & 1 & 1-\gamma \\ -\alpha_f\omega^2 h^2 & -\alpha_f 2\varepsilon\omega h & -\alpha_m \end{pmatrix} \quad (11)$$

The amplification matrix is finally given by:

$$\mathbf{A} = \mathbf{E}^{-1}\mathbf{B} \quad (12)$$

In order to avoid inverting the matrix $\mathbf{E}$, the eigenvalues of the amplification matrix $\mathbf{A}$ are obtained knowing that the roots of $\det|\mathbf{A} - \lambda\mathbf{I}|$ are the same as those of $\det|\mathbf{E}\lambda - \mathbf{B}|$ [25]. After calculations, the following characteristic equation which possesses three roots is found:

$$\begin{aligned} \det|\mathbf{E}\lambda - \mathbf{B}| = (\lambda-1)(\lambda-1)[(1-\alpha_m)\lambda + \alpha_m] \\ +[(1-\alpha_f)\lambda + \alpha_f]\,\omega^2 h^2\,[\gamma\lambda + (1-\gamma) \\ +(\lambda-1)[\beta\lambda + (0.5-\beta)]] \\ +[(1-\alpha_f)\lambda + \alpha_f]\,2\varepsilon\omega h\,[\gamma\lambda + (1-\gamma)](\lambda-1) \end{aligned} \quad (13)$$

This equation is then solved in order to study the evolution of the spectral radius with respect to the dimensionless product ωh for several values of the numerical damping ρ_∞ and of the structural damping ε.

V.I Analytical solution

The amplification matrix $\mathbf{A}$ calculated for the generalized-α method can be compared to its exact expression $\mathbf{A}^{exact}$ since the equation of motion Eq. (8) possesses an analytical solution. The goal is then to find $\mathbf{A}^{exact}$ such that:

$$\begin{pmatrix} q_{n+1} \\ h\dot{q}_{n+1} \end{pmatrix} = \mathbf{A}^{exact}(h, \omega, \varepsilon) \begin{pmatrix} q_n \\ h\dot{q}_n \end{pmatrix} \quad (14)$$

knowing that the solution of Eq. (8) has the following form if $\varepsilon < 1$:

$$q_{n+1} = e^{-\varepsilon\omega h}(C_1 \cos\omega_d h + C_2 \sin\omega_d h) \tag{15}$$

with the following parameters:

$$\omega_d = \omega\sqrt{1-\varepsilon^2} \tag{16}$$
$$C_1 = q_n \tag{17}$$
$$C_2 = \frac{1}{\omega\sqrt{1-\varepsilon^2}}(\dot{q}_n + \varepsilon\omega q_n) \tag{18}$$

After some calculations, the four components of the matrix $\mathbf{A}^{exact}$ are found:

$$A_{11}^{exact} = e^{-\varepsilon\omega h}\left[\cos(\sqrt{1-\varepsilon^2}\omega h) + \frac{\varepsilon\sin(\sqrt{1-\varepsilon^2}\omega h)}{\sqrt{1-\varepsilon^2}}\right] \tag{19}$$

$$A_{12}^{exact} = e^{-\varepsilon\omega h}\frac{\sin(\sqrt{1-\varepsilon^2}\omega h)}{\omega h\sqrt{1-\varepsilon^2}} \tag{20}$$

$$A_{21}^{exact} = -e^{-\varepsilon\omega h}\frac{\omega h\sin(\sqrt{1-\varepsilon^2}\omega h)}{\sqrt{1-\varepsilon^2}} \tag{21}$$

$$A_{22}^{exact} = e^{-\varepsilon\omega h}\left[\cos(\sqrt{1-\varepsilon^2}\omega h) - \frac{\varepsilon\sin(\sqrt{1-\varepsilon^2}\omega h)}{\sqrt{1-\varepsilon^2}}\right] \tag{22}$$

In the particular case where the structural damping is equal to $\varepsilon = 1$, the solution of the equation of motion is:

$$q_{n+1} = e^{\varepsilon\omega h}(C_1 + C_2 h) \tag{23}$$

with the two constants:

$$C_1 = q_n \tag{24}$$
$$C_2 = \dot{q}_n + \omega q_n \tag{25}$$

Thus, the components of the new exact amplification matrix $\mathbf{A}_{\varepsilon=1}^{exact}$ are the following:

$$\mathbf{A}_{\varepsilon=1}^{exact} = e^{-\varepsilon\omega h}\begin{pmatrix} 1+\omega h & 1 \\ \omega h(1-\varepsilon-\varepsilon\omega h) & 1-\varepsilon\omega h \end{pmatrix} \tag{26}$$

These two matrices are characterised by two eigenvalues. The spectral radius is then given by:

$$\rho = \max(|\lambda_1|, |\lambda_2|) \tag{27}$$

As in the numerical model, its evolution with respect to the dimensionless product ωh will be studied for several values of the structural damping ε.

V.II Comparison between the analytical and numerical solutions

In the model of a real structure, the frequency content can be divided into three parts. First, the low frequency domain such that $\omega h \lesssim 0.5$, for which the numerical simulation should be accurate in order to have a good representation of the physical behaviour. It implies that the damping introduced in the model should be a good approximation of the real damping.

Then, the second part is defined by high frequency modes such that $\omega h \gtrsim 2$. For this range of the spectrum, some dissipation must be present for purely numerical reasons. Indeed, it guarantees the convergence of the algorithm and a solution that is unaffected by the poorly represented modes of this domain.

Finally, the last part contains the intermediate frequencies for which a reasonable compromise must be found to ensure a smooth transition between low and high frequency domains.

In order to determine how the evolution of the spectral radius is affected by the structural and numerical dampings in the mass-spring-damper system, the analytical and numerical solutions are compared for several combinations of the damping parameters (Figure 7).

It can be seen in Figure 7a that when no structural damping ($\varepsilon = 0$) is present in the model, the spectral radius stays obviously equal to unity over the whole frequency domain and this behaviour is numerically recovered when there is no numerical damping ($\rho_\infty = 1$). Furthermore, this figure also highlights the effects of performing simulations with numerical damping only. As expected, the decrease in the spectral radius is sharper in the high frequency domain when ρ_∞ gets closer to zero, leading thus to a higher dissipation of its content, while on the opposite, the low frequency response remains unaffected.

If some structural damping is now introduced, the analytical solution follows an evolution characterised by the three parts mentioned previously (Figures 7b, 7c and 7d): a low frequency domain, a high frequency domain and an intermediate zone. Regarding the numerical curves, they first coincide with the analytical one in the low frequency domain as required. The curves tend to remain superimposed on a larger frequency range when the structural damping is high and the numerical damping is low. On the opposite, in the high frequency domain, they clearly diverge from the analytical solution, especially when the numerical damping is low. Moreover, the curves always converge to the value imposed by the numerical damp-

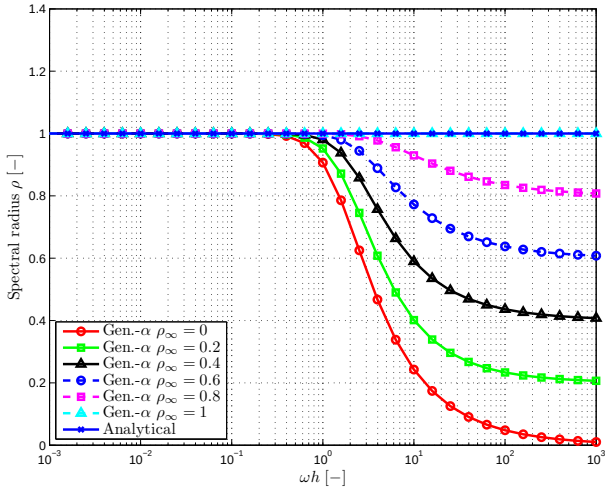

(a) Damping parameters: $\varepsilon = 0, 0 \leq \rho_\infty \leq 1$

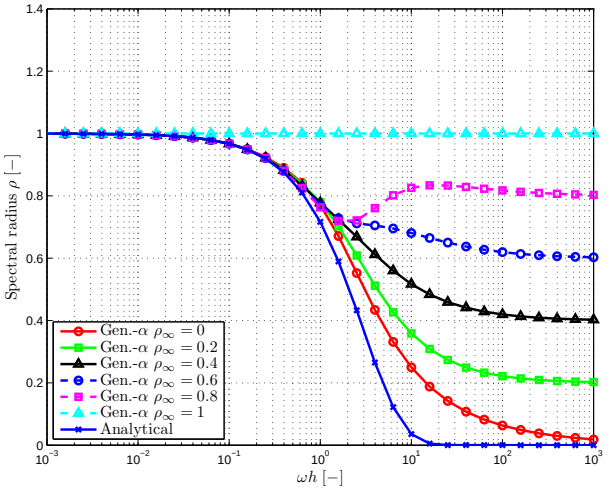

(b) Damping parameters: $\varepsilon = 1/3, 0 \leq \rho_\infty \leq 1$

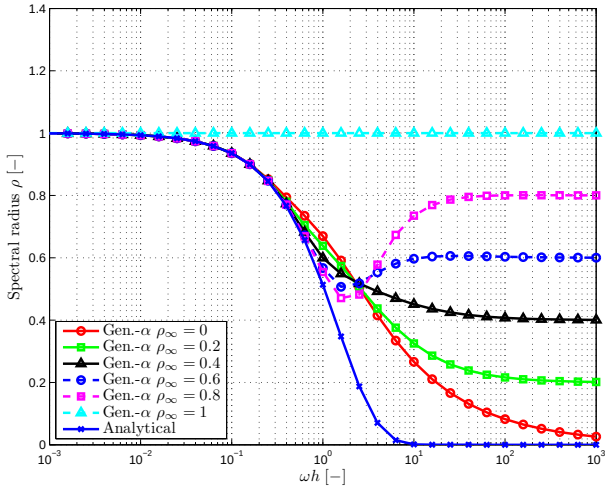

(c) Damping parameters: $\varepsilon = 2/3, 0 \leq \rho_\infty \leq 1$.

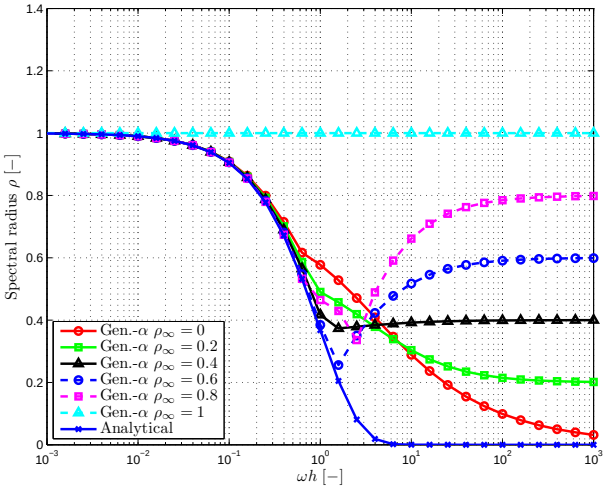

(d) Damping parameters: $\varepsilon = 1, 0 \leq \rho_\infty \leq 1$.

Figure 7: Comparison between the analytical solution of the equation of motion (8) and the resolution with the generalized-α method for several combinations of the damping parameters.

ing ρ_∞. Thus, it proves that in the numerical model the structural damping cannot provide the desired dissipation properties on this part of the frequency domain.

It can be observed that the curve related to $\rho_\infty = 0$ is the only one to converge to the same value as the analytical solution in high frequencies. However, other values of ρ_∞ are equally acceptable because accuracy is not sought in this part of the domain. Indeed, the only important factor is the amount of dissipation that is required to ensure the convergence of the solution.

To conclude, in order to have a valid numerical solution, a correct representation of the structural damping is needed in the low frequency range and some numerical damping should be introduced to filter the undesired high frequency spurious modes. These conclusions concern a simple yet representative linear problem, while in tape springs, the nonlinearities give rise to more complex behaviours such as couplings and transfers of energy between the low and high frequencies. The objective of Sections VI and VII is then to extend the analysis to the

numerical and structural dampings in tape spring simulations based on finite element tests.

VI IMPACT OF THE NUMERICAL DAMPING ON THE DYNAMIC BEHAVIOUR OF TAPE SPRINGS

In order to determine the impact of the numerical damping on the dynamic behaviour of tape springs, a model is solved several times with different values of ρ_∞, but without any structural damping. The pattern described in Section III is followed: first, the tape spring is folded in the opposite sense until the bending angle reaches 60°, then the structure is released and its dynamic behaviour is analysed for 110 *s*. Furthermore, in order to simplify the behaviour in the equal sense bending and reduce the impact of the torsion, the displacements in the transverse direction are locked on the whole length of the median. The structure consists of a long tape spring, the properties of which are the same as in Table 1, but with a length L of 400 *mm*. Regarding the boundary conditions, it is clamped on one extremity and rigidly connected to a lumped mass of 0.5 *kg* on the other one (Figure 8). The purpose of this lumped mass is to simulate the deployment and the inertia of an appendix.

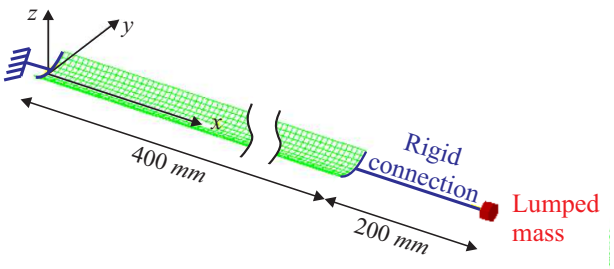

Figure 8: Tape spring with the properties of Table 1 but with a length of 400 *mm* rigidly connected to a lumped mass (0.5 *kg*).

The evolution of the bending moment for this model with $\rho_\infty = 0.2$ is given in Figure 9. Notice that in this case the x-axis is the elapsed time of the simulation since a dynamic analysis is performed. Nonetheless, as the first part (from 0 to 60 *s*) is very slow and corresponds to the folding with a constant bending velocity, the time is directly related to the bending angle as in Figure 4.

Furthermore in this part, the numerical damping has a low impact on the value of the peak moment $M_+^{\max}$ and the residual moment M_+^* as it can be seen in the first two plots of Figure 10. However, as it can be expected, a reduction of the numerical damping implies longer periods of oscillations after the buckling around 10.4 *s* since the

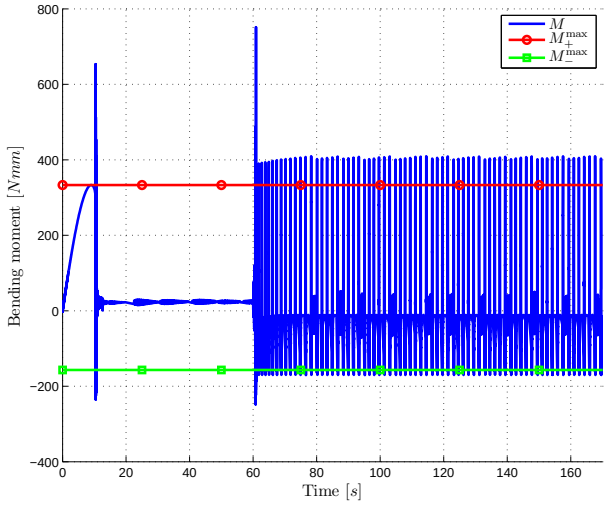

Figure 9: Bending moment evolution for the tape spring of Figure 8 with $\rho_\infty = 0.2$.

dissipation in the system is less effective. Thus, Figure 10 (third plot) gives the time at which the difference between the bending moment and the residual moment determined in the second plot of Figure 10 reaches less than 10 %. Between the two extreme situations with $\rho_\infty = 0.2$ and $\rho_\infty = 0.8$, an increase in time of 24.83 % is noticed. For the latter value, the associated results were obtained after a CPU time of 153 hours, therefore simulations for which $\rho_\infty > 0.8$ were not performed.

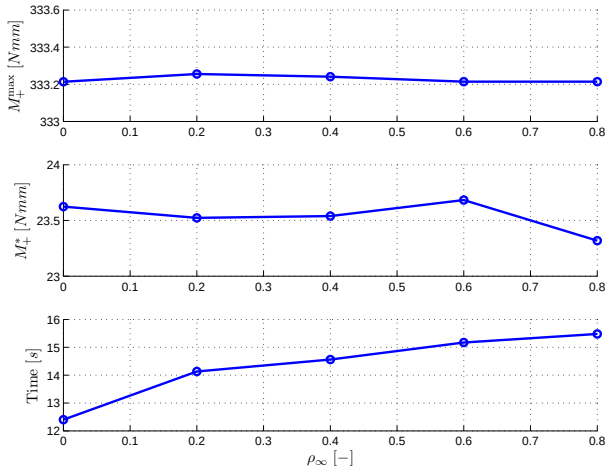

Figure 10: Peak moment $M_+^{\max}$, residual moment M_+^* and duration of the oscillations after buckling for several values of the numerical damping ρ_∞.

In the strictly dynamic part of the simulation (from 60 to 170 s), the deployment of the tape spring leads to large asymmetric oscillations submitted to very low damping whatever the value of ρ_∞ (Figure 9). On that same figure, it can be seen that the limits defined by the peak moments $M_+^{\max}$ and $M_-^{\max}$ are both exceeded which is due to dynamic effects. In order to check whether a fold is created or not, the flattening of the cross-sections is analysed at each time step by computing their curvature. A fold is then considered created when the curvature is lower than $10^{-2}\ mm^{-1}$ which is the value reached at the beginning of the buckling in the quasi-static analysis. The folded configuration is such that there is never more than one fold in the structure at a given time instant. The results are represented in Figure 11 which shows the evolution of the vertical displacement at the tip of the tape spring during deployment starting from the folded configuration. The plot stops at 100 s for more clarity. Superimposed to the black curve, a dot is drawn for each time step. It can be seen that, during the oscillations, red dots are only associated to positive vertical displacements, which means that the formation of folds only occurs in the equal sense.

It can be concluded that when the dissipation in the system is only characterised by numerical damping, the behaviour in the quasi-static analysis is well represented. Furthermore, in the dynamic analysis, the nonlinear oscillations are only slightly damped because they occur in the low frequency range, i.e. out of the range of influence of the numerical damping.

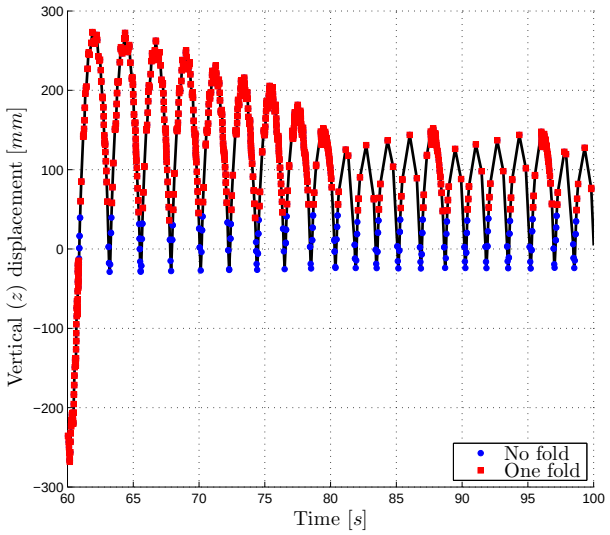

Figure 11: Vertical displacement of the tip of the tape spring with $\rho_\infty = 0.2$ and existence of folds.

VII INTRODUCTION OF STRUCTURAL DAMPING IN THE TAPE SPRING MODEL

As it was shown analytically in Section V on a simple one-degree-of-freedom system and numerically in the previous section on a complete tape spring with an appendix, the behaviour of a model cannot be precisely predicted by introducing only numerical damping. Thus, some structural damping is now added in the finite element model described in Figure 8. In order to keep the simulations as simple as possible, the dissipation is represented by Kelvin-Voigt models, which involve a Young modulus E and a viscosity coefficient η acting in parallel and correspond to viscoelastic solids [26].

The evolution of the bending moment during the folding and the deployment is given in Figure 12 for $\rho_\infty = 0.2$ and $\eta = 10^{-3}\ s$. Compared to the previous situations without any structural damping, the following elements are noticeable. First, the peak moment $M_+^{\max}$ is barely affected by this new damping (Figure 13, first plot). Then, right after the buckling, the amplitude of the oscillations is much smaller, as well as their duration which is quasi independent from the numerical damping (Figure 14, first plot). During the stabilisation, the residual moment M_+^* has a better convergence and is also less dependent on the numerical damping (Figure 13, second plot).

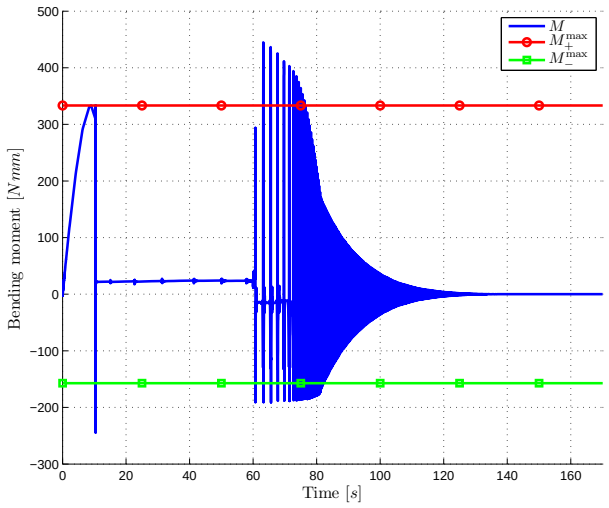

Figure 12: Bending moment evolution for the tape spring of Figure 8 with $\rho_\infty = 0.2$ and $\eta = 10^{-3}\ s$.

Finally, the oscillations after deployment are damped out and, although their duration naturally increases when the numerical damping decreases, the difference between the extreme situations is only of 9.4 % if the oscillations

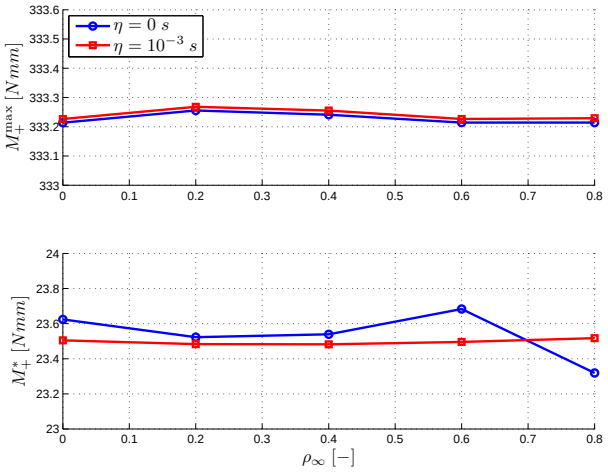

Figure 13: Peak moment $M_+^{\max}$ and residual moment M_+^* for several values of the numerical damping ρ_∞.

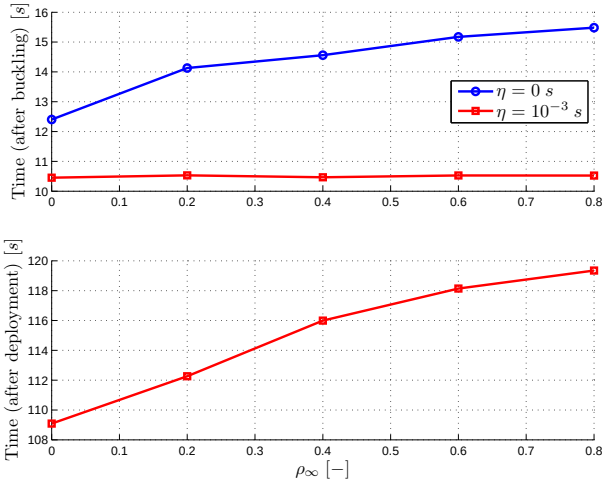

Figure 14: Duration of the oscillations after buckling and after the release of the tape spring for several values of the numerical damping ρ_∞.

are considered as negligible when they reach $\pm 10\,N/mm$. As it was the case in the previous section, the limits defined by the peak moments $M_+^{\max}$ and $M_-^{\max}$ are both overshot due to dynamic effects, but only folds in the equal sense bending are formed as it can be seen in Figure 15. Furthermore, the dynamic response can be divided into two parts based on the evolution of the amplitudes. First, from 60 to $\sim 80\ s$ (Figure 12), the oscillations are asymmetric due to the creation of a fold in equal sense bending and they are submitted to a nonlinear damping. Then, from ~ 80 to $140\ s$, the structure does not fold anymore and thus behaves almost linearly. The oscillations are then symmetric with an exponential decrease. If the same zones are analysed in the evolution of the vertical tip displacement of the tape spring (Figure 15), it can be seen that the first part is associated with a sharp reduction of the motion amplitude, followed by an exponential decrease in the second zone. It proves then that the self-locking phenomenon occurs and strongly helps to the stabilisation of the structure in its fully deployed state as expected in experimental applications [7].

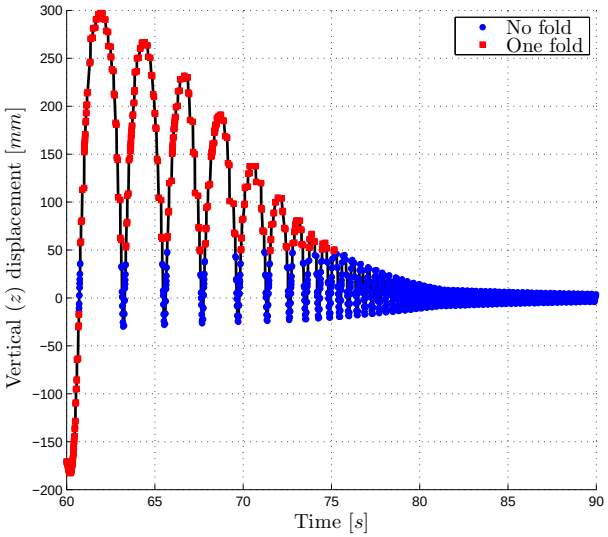

Figure 15: Vertical displacement of the tip of the tape spring with $\rho_\infty = 0.2$ and $\eta = 10^{-3}\ s$ and existence of folds.

VIII CONCLUSIONS

The purpose of this paper is to determine the impact of the numerical and the structural dampings in a dynamic analysis involving the folding and the deployment of a specific type of compliant structures: tape springs.

First, it is shown on a simple one-degree-of-freedom system that the simulation procedure used to solve the finite element models requires the two types of damping to obtain a valid numerical solution. Indeed, on the one hand, in order to have some dissipation in the high frequency domain, some numerical damping must be introduced. It guarantees the convergence of the algorithm and a solution that is unaffected by the poorly represented modes of this domain. Then, on the other hand, regarding the low frequency content, some structural damping is needed in order to have a good representation of the real damping and of the physical behaviour of the system.

Those conclusions are then exploited in a practical case which consists of the finite element model of a long tape spring rigidly connected to an appendix. It is shown that the introduction of structural damping allows reducing the dependence of the characteristic features to the amount of numerical damping and, most importantly, ensures a correct representation of the damping of the oscillations after deployment and of the self-locking of the structure in the fully deployed state. The structural dissipation model chosen in the finite element analyses is the Kelvin-Voigt model. We expect that similar conclusions could be obtained for other dissipation models. Further works will address the selection of the most representative dissipation model for a given tape spring design and its experimental validation.

Acknowledgement

The first author would like to acknowledge the Belgian National Fund for Scientific Research for its financial support.

References

[1] S. Pellegrino. Deployable Structures in Engineering. *Deployable Structures*, CISM courses and lectures 412, Springer, 2001.

[2] K. A. Seffen. Analysis of Structures Deployed by Tape-Springs. *Ph. D. thesis*, Cambridge University, United-Kingdom, 1997.

[3] W. Wüst. Einige Anwendungen des Theorie der Zylinderschale. *Zeitschrift für Angewandte Mathematik und Mechanik*, **34**, 444–454, 1954.

[4] F. P. J. Rimrott. Querschnittsverformung bei Torsion offener Profile. *Zeitschrift für Angewandte Mathematik und Mechanik*, **50**, 775–778, 1970.

[5] E. H. Mansfield. Large-deflexion torsion and flexure of initially curved strips. *Proceedings of the Royal Society of London*, Vol. **A 334**, 1125–1132, 1973.

[6] K. A. Seffen, S. Pellegrino. Deployment of a rigid panel by tape-springs. *Department of Engineering, University of Cambridge, Report CUED/D-STRUCT/TR168.*, 1997.

[7] K. A. Seffen, S. Pellegrino. Deployment Dynamics of Tape-Springs. *Proceedings of the Royal Society of London*, Vol. **A 455**, 1003–1048, 1999.

[8] F. Guinot, S. Bourgeois, B. Cochelin, L. Blanchard. A planar rod model with flexible thin-walled cross-sections. Application to the folding of tape springs. *International Journal of Solids and Structure*, Vol. **49 (1)**, 73–86, 2012.

[9] K. A. Seffen. On the Behaviour of Folded Tape-Springs. *ASME Journal of Applied Mechanics*, Vol. **68**, 369–375, 2001.

[10] S. J. I. Walker, G. Aglietti. Study of the Dynamics of Three-Dimensional Tape Spring Folds. *AIAA Journal*, Vol. **42**, 850–856, 2004.

[11] S. J. I. Walker, G. Aglietti. Experimental Investigation of Tape Springs Folded in Three Dimensions. *AIAA Journal*, Vol. **44**, 151–159, 2006.

[12] S. J. I. Walker, G. Aglietti. A study of tape spring fold curvature for space deployable. *Proceedings of the Institution of Mechanical Engineers, Part G: Journal of Aerospace Engineering*, 313–325, 2007.

[13] Ö. Soykasap. Analysis of tape spring hinges. *International Journal of Mechanical Sciences*, Vol. **49**, 853–860, 2007.

[14] D. Givois, J. Sicre, . Mazoyer. A low cost hinge for appendices deployment: design, test and application. *9th European Space Mechanisms and Tribology Symposium*, Liège, Belgium, 19-21 September 2001.

[15] J. Sicre, D. Givois, E. Emerit. Application of Maeva hinge to myriade microsatellites deployments needs. *11th European Space Mechanisms and Tribology Symposium/ESMATS 2005, ESA/ CNES*, Lucerne, Suisse, 21–23 September 2005.

[16] S. Hoffait, O. Brüls, D. Granville, F. Cugnon, G. Kerschen. Dynamic analysis of the self-locking phenomenon in tape-spring hinges. *Acta Astronautica*, Vol. **66**, 1125–1132, 2010.

[17] K. Kwok, S. Pellegrino. Viscoelastic Effects in Tape-Springs. *52nd AIAA/ASME/ASCE/ AHS/ASC Structures, Structural Dynamics and Materials Conference*, Denver, CO, 4-7 April 2011.

[18] M. Mobrem, D. Adams. Deployment Analysis of Lenticular Jointed Antennas Onboard the Mars Express Spacecraft. *Journal of Spacecraft and Rockets*, Vol. **46**, 394–402, 2009.

[19] K. A. Seffen, Z. You, S. Pellegrino. Folding and deployment of curved tape springs. *International Journal of Mechanical Sciences*, Vol. **42**, 2055–2073, 2000.

[20] S.A. Samtech, SAMCEF user manual, Version 8.4, 2013.

[21] N. Newmark. A method of computation for structural dynamics. *ASCE Journal of the Engineering Mechanics Division*, Vol. **85**, 67–94, 1959.

[22] H. Hilber, T. Hughes, R. Taylor. Improved numerical dissipation for time integration algorithms in structural dynamics. *Earthquake Engineering and Sructural Dynamics*, Vol. **5**, 283–292, 1977.

[23] J. Chung, G. Hulbert. A time integration algorithm for structural dynamics with improved numerical dissipation: the generalized-α method. *ASME Journal of Applied Mechanics*, Vol. **60**, 371–375, 1993.

[24] C. Calladine. The theory of thin shell structures. *Proceedings of the Institution of Mechanical Engineers, Part A: Journal of Power and Energy*, Vol. **202**, 141–149, 1988.

[25] M. Géradin, A. Cardona. Flexible Multibody Dynamics, A Finite Element Approach. *Wiley*, 2001.

[26] R. M. Christensen. Theory of Viscoelasticity: An Introduction. *Academic Press*, 1971.